Directional and Spectral Control of Thermal Emission and Its Application in Radiative Cooling and Infrared Light Sources

Yurui Qu,[1,2,3] Meiyan Pan,[3] and Min Qiu[1,2,*]

[1] *Key Laboratory of 3D Micro/Nano Fabrication and Characterization of Zhejiang Province, School of Engineering, Westlake University, 18 Shilongshan Road, Hangzhou, 310024 Zhejiang, China*

[2] *Institute of Advanced Technology, Westlake Institute for Advanced Study, 18 Shilongshan Road, Hangzhou, 310024 Zhejiang, China*

[3] *State Key Laboratory of Modern Optical Instrumentation, College of Optical Science and Engineering, Zhejiang University, Hangzhou, 310027 Zhejiang, China*

(Received 23 November 2019; revised manuscript received 17 March 2020; accepted 15 May 2020; published 22 June 2020)

The ability to control the directional and spectral properties of thermal emission is of fundamental importance for many applications. Here we propose a method to design directional and broadband thermal emitters (DBTEs) and directional and narrowband thermal emitters (DNTEs) based on classic thermal emitters and angular selectors. DBTEs exhibit strong thermal emission at a specific angle and within a broadband wavelength range. Besides, DBTEs achieve better radiative cooling performance than classic thermal emitters without special angular control when there are surrounding buildings. On the other hand, DNTEs can confine thermal emission within a narrow bandwidth and a narrow angular width. DNTEs show higher energy conversion efficiency than conventional narrowband thermal emitters, and have potential application in high-efficiency infrared light sources.

DOI: 10.1103/PhysRevApplied.13.064052

I. INTRODUCTION

Thermal emission from opaque materials, such as a black body or an incandescent source, has long been regarded as an incoherent phenomenon due to the uncorrelated properties of spontaneous emission. About two decades ago, temporally and spatially coherent thermal emitters were theoretically and experimentally demonstrated [1,2]. Since then, different methods to control and manipulate thermal emission based on nanostructures have been developed. Most studies focus on control of the spectral properties of thermal emission, which spawns a myriad of applications, such as radiative cooling [3–7], thermophotovoltaic devices [8–10], and thermal camouflage [11–14]. In contrast, there are few studies on the directional control of thermal emission. However, the directional control of thermal emission is of vital importance in fundamental science and a number of applications [15,16], and needs to be further investigated.

Thermal emitters can be divided into five categories on the basis of their different spatial and spectral properties, as shown in Fig. 1. Wide-angle and broadband thermal emitters, for example, a black body, photonic crystals [3], glass-polymer hybrid metamaterial [4], and refractory-metal based metamaterial [17]. Wide-angle and narrowband thermal emitters such as metal-insulator-metal structures [18–20]. The thermal emission is confined in a narrow wavelength range but within a wide-angle range. Spatially and temporally coherent thermal emitters are quasidirectional and narrowband thermal emitters because the thermal emission is directional at some specific wavelength and narrowband in some specific direction. Several structures such as gratings [2,21] and vertical-cavity enhanced resonant thermal emitters [22] have been proposed to control the thermal emission spatially and temporally. A one-dimensional (1D) photonic crystal with a polar material as a coating layer is also proposed to achieve highly spectral and directional thermal emission [23]. However, the thermal emission of spatially and temporally coherent thermal emitters is still within a large angular and wavelength range, unlike directional and narrowband thermal emitters (DNTEs), which confine thermal emission within a narrow bandwidth and narrow angular width (Fig. 1).

Several strategies to achieve directional and broadband thermal emitters (DBTEs) and DNTEs have also been investigated. Hyperbolic materials of type II have been demonstrated to generate directional and broadband thermal emission, but the emission angular width is quite large (more than 20°) [24]. For semitransparent plane-parallel semiconductor layers, the emission spectrum is broadband

*qiu_lab@westlake.edu.cn

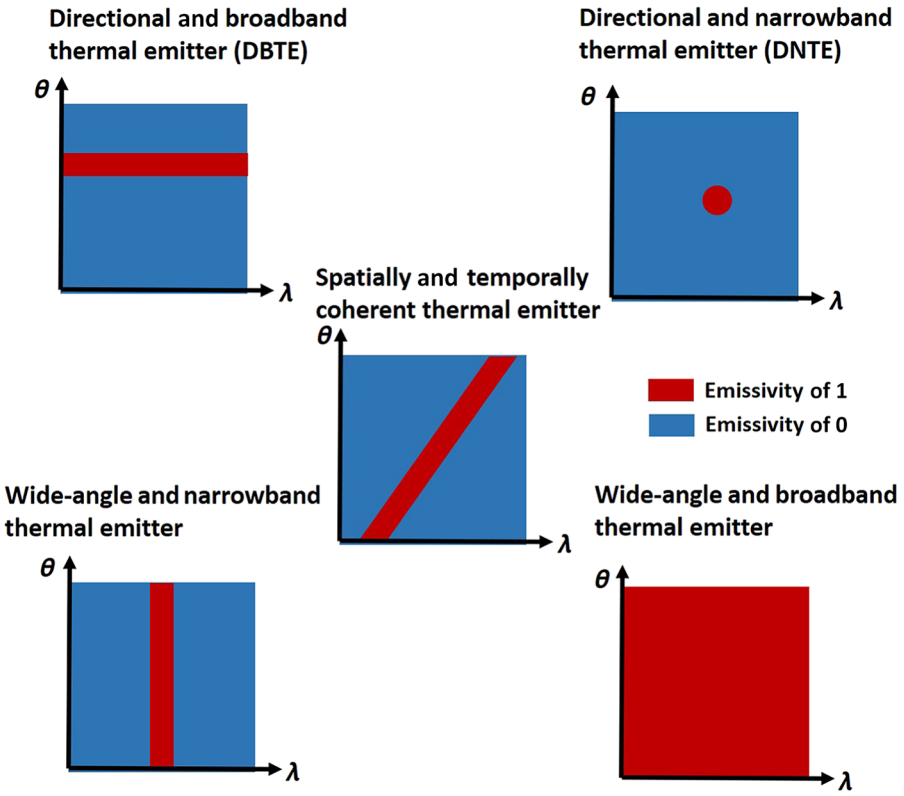

FIG. 1. Five kinds of thermal emitters with different spatial and spectral properties. A wide-angle and broadband thermal emitter (e.g., a black body), a wide-angle and narrowband thermal emitter (e.g., a metal-insulator-metal structure), and a spatially and temporally coherent thermal emitter (e.g., a grating) have been demonstrated. However, achieving a directional and broadband thermal emitter and a directional and narrowband thermal emitter has remained elusive so far.

and the emission angle is partially directional. However, the emissivity is only around 0.5 and the emission angular distribution is still broad from 0° to 60° for a Si plate [25]. Plasmonic Brewster funneling and adiabatic focusing have been combined to achieve ultrabroadband omnidirectional thermal emission, but the emission angle is larger than 80° [26]. On the other hand, some progress has been made toward achieving DNTEs such as plasmonic metasurfaces [16] and metallic bull's eyes [27]. However, they require nanofabrication methods such as electron-beam lithography and cannot be easily scaled up. An approach using two-dimensional photonic crystals combined with quantum wells was proposed [15], but the angular range of thermal emission is large (from −20° to 20°) and the central wavelength is fixed due to the intrinsic intersubband transitions of multiple quantum wells. Campione *et al*. [28] used semiconductor hyperbolic metamaterial to control the emission angle and wavelength simultaneously. However, the angular range of thermal emission was larger than 40° and the peak emissivity was low (approximately 0.4). Zhu *et al*. [29] designed a structure in which a single layer of two-dimensional material is separated from a mirror by a dielectric spacer layer. The drawback is the central emission angle is nearly 90°.

In this work, we design two kinds of thermal emitters, a DBTE and a DNTE, based on classic thermal emitters and angular selectors. The past few years have witnessed great strides made in the field of angular selectivity [30,31]. Angular selectivity can select light on the basis of the light propagation direction and was recently applied to high-efficiency solar-energy conversion [32,33], privacy protection [34,35], and detectors with enhanced signal-to-noise ratios [36]. Here we propose applying angular selectivity to classic thermal emitters to control the spatial and temporal properties of thermal emission simultaneously. For the DBTE, we design a material system consisting of an angular selector on top of a broadband thermal emitter. Such a thermal emitter can emit in a specific direction within a broadband wavelength range, which can be used for directional radiative cooling when there are surrounding buildings. For the DNTE, we propose a structure consisting of an angular selector on top of a vertical-cavity enhanced resonant thermal emitter. The DNTE can emit at a specific wavelength of 3.92 μm with a bandwidth of about 0.04 μm and a specific angle of 61° with an angular width of around 5°. Compared with a conventional narrowband thermal emitter, the DNTE can achieve a higher equilibrium temperature and higher energy-conversion efficiency. This method based on angular selectivity will pave the way toward the spatial and spectral control of thermal emission in both the fundamental-science field and a number of energy-harvesting applications.

II. DIRECTIONAL AND BROADBAND THERMAL EMITTER

A. Structure and emissivities of the DBTE

We first show how to achieve a DBTE. First, we achieve broadband angular selectivity on the basis of the fact that (i) p-polarized light transmits without any reflection at the Brewster angle and (ii) the band gaps of photonic crystals can prevent light propagation for given frequency ranges and the band gaps can be broadened [30]. We consider a simple 1D photonic crystal consisting of materials A and B with period a_i of the ith stack and relative permittivities ε_A and ε_B, as shown in Fig. 2(a). In such a system, monochromatic plane waves with a specific frequency can propagate only in a certain direction; propagation in other directions is not allowed because of destructive interference (also known as photonic band gaps). However, for p-polarized light, there is a special propagation angle, known as the Brewster angle,

$$\theta_B = \tan^{-1}\sqrt{\frac{\varepsilon_A}{\varepsilon_B}}, \tag{1}$$

where θ_B is the Brewster angle in the layers with permittivity ε_A. At θ_B, p-polarized light is totally transmitted for all frequencies. First, BaF_2 and ZnS are chosen as the materials for the 1D photonic crystals because they are transparent in the mid-infrared range. The permittivities of the materials are described in detail in Appendix A. For index-matching purposes, the light is incident from a medium with refractive index $n = 1.4$. The thickness of the BaF_2 and ZnS layers in the first stack is a_0, and r is the geometric series of the periods of these stacks as $a_i = a_0 r^{i-1}$. Here we choose proper parameters $a_0 = 390$ nm and $r = 1.02$. The film thickness of the thermal emitter is proportional to the emission wavelength, so a_0 is chosen to ensure it is the smallest value to cover the whole spectral range. Parameter r cannot be too small or too large. If r is too small, the angular selector cannot cover the whole wavelength range. If r is too large, there will be some "leaky" thermal emission around the emission angle because the extended modes are allowed to propagate between two band gaps.

Next we consider that materials A and B are isotropic and anisotropic materials. Such isotropic-anisotropic bilayers can be obtained with use of widely used polymers [37,38] and mature mechanical methods in industry [39–42]. One widely used method called "multilayer coextrusion" has been used to form thousands of layers of two alternating materials [43–46]. Multilayer coextrusion uses a process of forced assembly through sequential layer multiplication to fabricate thin alternating layers of two or three materials. Such a method can produce multilayer

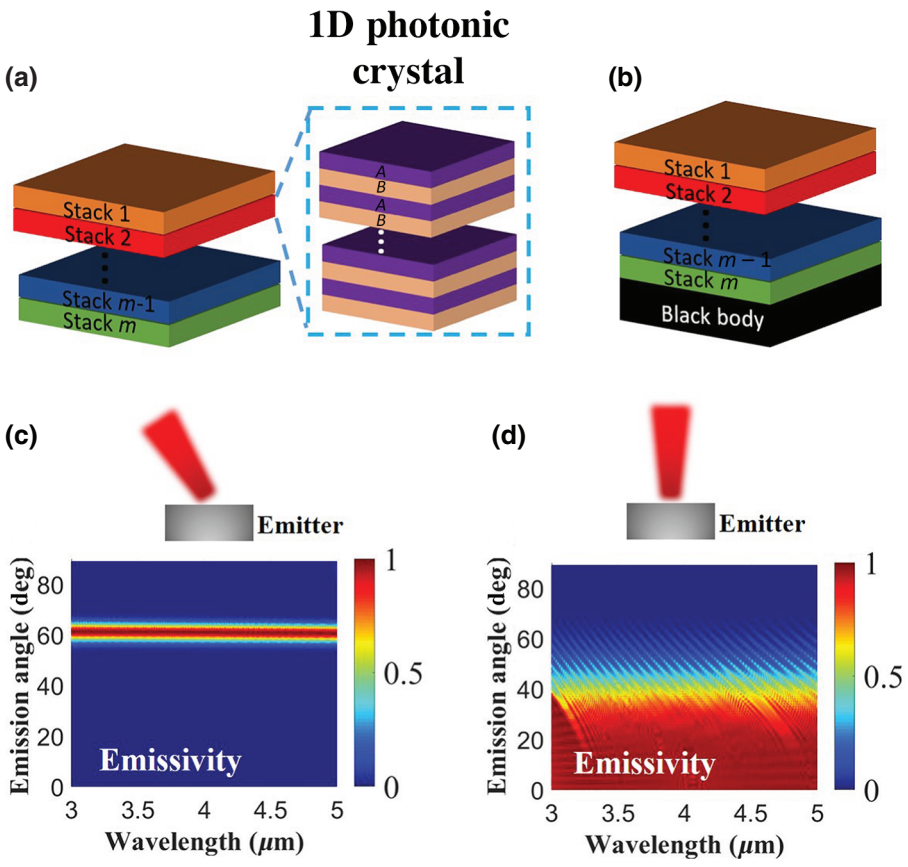

FIG. 2. (a) Quarter-wave stacks consisting of two materials A and B. (b) DBTE based on an angular selector on top of a black body. (c) p-polarized emissivities of materials BaF_2 and ZnS with 50 stacks, each stack consisting of eight bilayers. (d) p-polarized emissivities of the anisotropic material nylon 6 and the isotropic material polysulfone with 35 stacks, each stack consisting of 50 bilayers.

films with thousands of layers. For example, a coextrusion process with 11 multiplier dies produced 4096 alternating polycarbonate (PC) and poly(methyl methacrylate) (PMMA) layers [47]. Here we choose polysulfone as the isotropic material with a refractive index of 1.62 [48], and oriented nylon 6 as the anisotropic material with an average in-plane refractive index of 1.62 and out-of-plane refractive index of 1.49 [37]. The transparent window of such a material system is centered at 0° because light "sees" the same refractive index of materials A and B at normal incidence and is totally transmitted. Broadband angular selectivity between 3 and 5 μm can be achieved. The effective band gaps can be increased when the quarter-wave stacks with various periods are piled (see Fig. S1 in Supplemental Material [49]). The simulation results for lossy polymer materials are also studied (see Fig. S2 in Supplemental Material [49]). Although the efficiency of the angular selecitivity is reduced, a directional and broadband angular selector can still be achieved.

We design two DBTE material systems based on the two broandband angular selectors mentioned above on top of a black body [Fig. 2(b)]. The black body can be replaced by any other kind of broadband thermal emitter. The black body exhibits strong thermal emission within a broandband wavelength range and in all directions. If the black body is covered with an angular selector, only thermal emission within a transparent window can escape outside and thermal emission from other angles is reflected back and reabsorbed by the bottom black body. A broadband (3–5 μm) and directional thermal emitter can be achieved, as shown in Figs. 2(c) and 2(d). The central emission angle can also be tuned by choosing different materials A and B. When the two materials are BaF_2 and ZnS, the central emission angle is 61° and the angular width is around 5°. If nylon 6 as an anisotropic material and polysulfone as an isotropic material are chosen, a thermal-emission window (0°–40°) can be achieved.

Although we focus here on control of thermal emission for one polarization, our approaches can be generalized to both polarizations. We demonstrate that the thermal emitter based on 1D anisotropic photonic crystal stacks has broadband and directional thermal emission for p polarization. A half-wave plate, which is one simple anisotropic layer, can convert s-polarized light to p-polarized light. By inserting half-wave plates between 1D photonic crystal stacks, we can achieve broadband and directional thermal emission for both polarizations (see Fig. S3 in Supplemental Material [49]). We also study full-space emissivities of DBTEs in polar coordinates (see Fig. S4 in Supplemental Material [49]). The emissivities are the same for different azimuths ϕ from 0° to 360° because the multilayer film is uniform in the plane.

B. Ideal model of radiative cooling based on angular selectivity when there are surrounding buildings

Radiative-cooling technology takes advantage of strong mid-infrared thermal emission in the transparent "atmospheric window" ranging from 8 to 14 μm and can

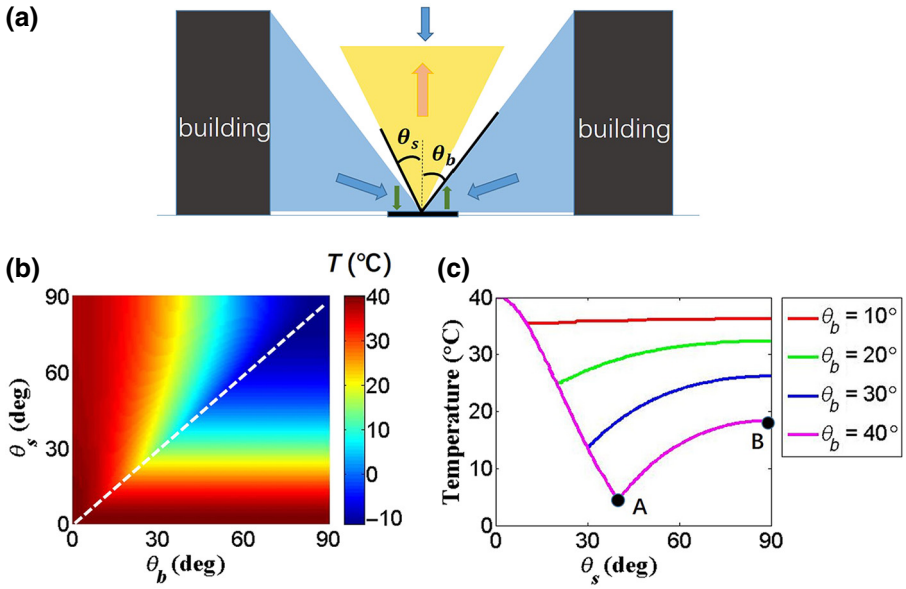

FIG. 3. (a) Radiative cooling with angular control of thermal emission when there are surrounding buildings. θ_s is the "thermal-emission window" of the sample and θ_b represents the height of surrounding buildings. (b) The equilibrium temperature of the DBTE sample for different values of θ_s and θ_b when the ambient temperature is 40 °C. The dashed white line represents the lowest cooling temperature after optimization of θ_s based on different θ_b. The conductive and convective loss can be quantified with use of the effective heat-transfer coefficient $h = 3\ \mathrm{W\,m^{-2}\,K^{-1}}$. (c) The equilibrium temperature of the DBTE sample for different thermal emission angles θ_s. Red, green, blue, and pink lines represent different values of θ_b as 10°, 20°, 30°, and 40°, respectively.

decrease the temperature of the object without any power consumption [3,4]. However, current radiative-cooling devices need to be installed on roofs because their performances will deteriorate if there are surrounding buildings. This greatly limits the applications of radiative cooling in a wide range of areas and places. A recently published paper proposed a method that can control the direction of thermal emission for radiative cooling [7]. This method uses geometric optics for control of the thermal-emission beam. Here we propose a method based on angular band gaps of 1D photonic crystals. Our material system with angular control can achieve a lower cooling temperature than classic radiative-cooling technology without any angular control.

We begin with an ideal model of a DBTE sample that is surrounded by the buildings in a circle. The cross section is shown in Fig. 3(a). For the wavelength ranging from 8 to 14 μm, the DBTE sample has 100% absorptivity and emissivity within its "emission window" ranging from 0° to θ_s [yellow-triangle region in Fig. 3(a)], and 100% reflectivity for other angles. The emissivity of the DBTE sample between 8 and 14 μm is given in Eq. (2):

$$\varepsilon_s(\theta) = \begin{cases} 1, & 0^\circ < \theta < \theta_s, \\ 0, & \theta_s < \theta < 90^\circ. \end{cases} \tag{2}$$

The emissivity of the sample is zero when the wavelength is less than 8 μm or greater than 14 μm. θ_b represents the height and distance of the adjacent buildings. The buildings contain steel and concrete, whose emissivities are very high. Here we assume that the emissivities of the surrounding buildings are 0.95. There is strong thermal emission from buildings to the radiative-cooling device within the "building's emission window" ranging from θ_b to 90° [blue region in Fig. 3(a)]. Most of the time, the temperature of the classic radiative-cooling device is lower than the temperature of the ambient atmosphere and surrounding buildings due to its radiative-cooling mechanism. The thermal emission absorbed by the classic radiative-cooling device without specific angular control (coming from the buildings) is greater than that emitted by the device. Therefore, the cooling efficiency is decreased. However, the DBTE-based radiative cooling can reflect the strong thermal emission from the surrounding buildings and achieve higher cooling efficiency than classic devices without angular control.

We calculate the equilibrium temperature of the ideal DBTE sample for different values of θ_s and θ_b, as shown in Fig. 3(b). Here we consider only night-time radiative cooling for simplicity. Daytime radiative cooling can also be achieved by adding an additional reflector for visible light. The energy flux of the DBTE sample contains three parts: thermal emission P_r, absorption from the atmosphere and buildings P_a, and conductive and convective loss P_c, which are described in detail in Appendix B. The equilibrium temperature can be calculated when the net power flux $P_{\text{net}} = P_a + P_c - P_r$ is zero. The dashed white line in Fig. 3(b) represents the lowest cooling temperature of the sample for different values of θ_s and θ_b. The results show that the lowest cooling temperature (also highest cooling efficiency) can be obtained when θ_s is close to θ_b. That makes sense because the best angular control of the sample is to reflect almost all strong thermal emission from the buildings and emit the energy itself to the sky as much as possible. For different values of θ_b, the equilibrium temperature of the sample decreases first when θ_s increases and then reaches a minimum when $\theta_s \approx \theta_b$ [Fig. 3(c)]. The temperature of the sample then increases as θ_s increases. The optimized θ_s (point A) can achieve a lower equilibrium temperature (higher cooling efficiency) than the classic radiative-cooling devices without angular control of thermal emission (point B).

C. Realistic model of radiative cooling based on angular selectivity when there are surrounding buildings

The key component of a classic radiative-cooling device is a broadband thermal emitter. Here we use a three-layer broadband thermal emitter consisting of Au, SiO_2, and Si_3N_4 films for comparison [Fig. 4(a)]. The thicknesses of the Au, SiO_2, and Si_3N_4 films are 100 nm, 1 μm, and 220 nm, respectively. Such a broadband thermal emitter has high emissivities between 8 and 14 μm and low emissivities at other wavelengths [Fig. 4(b)]. The broadband thermal emitter has no special angular control of thermal emission, and thus the emissivities remain high even when the emission angle increases to 85°. The relation between the height and the distance of buildings is regulated in law in China to ensure of enough sunshine time and θ_b has to be larger than 30°. Here we assume that θ_b is 40°.

The DBTE is designed by our placing a multilayer angular selector on top of the three-layer broadband thermal emitter [Fig. 4(c)]. When materials A and B of the bilayers are both isotropic materials, the emission angle can only be at the Brewster angle, which is larger than 45°. However, emission angles ranging from 0° to 40° are required for radiative cooling with surrounding buildings. Therefore, anisotropic material A and isotropic material B with the above-mentioned permittivities are chosen as the materials for the angular selector. We consider an angular selector of 160 stacks, each stack consisting of 60 isotropic-anisotropic bilayers. The periods of these stacks form a geometric series $a_i = a_0 r^{i-1}$ with $r = 1.01$. The thicknesses of layers A and B in the first stack are 1 μm ($a_0 = 1$ μm). Such a DBTE has high emissivity when the emission angle ranges from 0° to 40° and nearly 100%

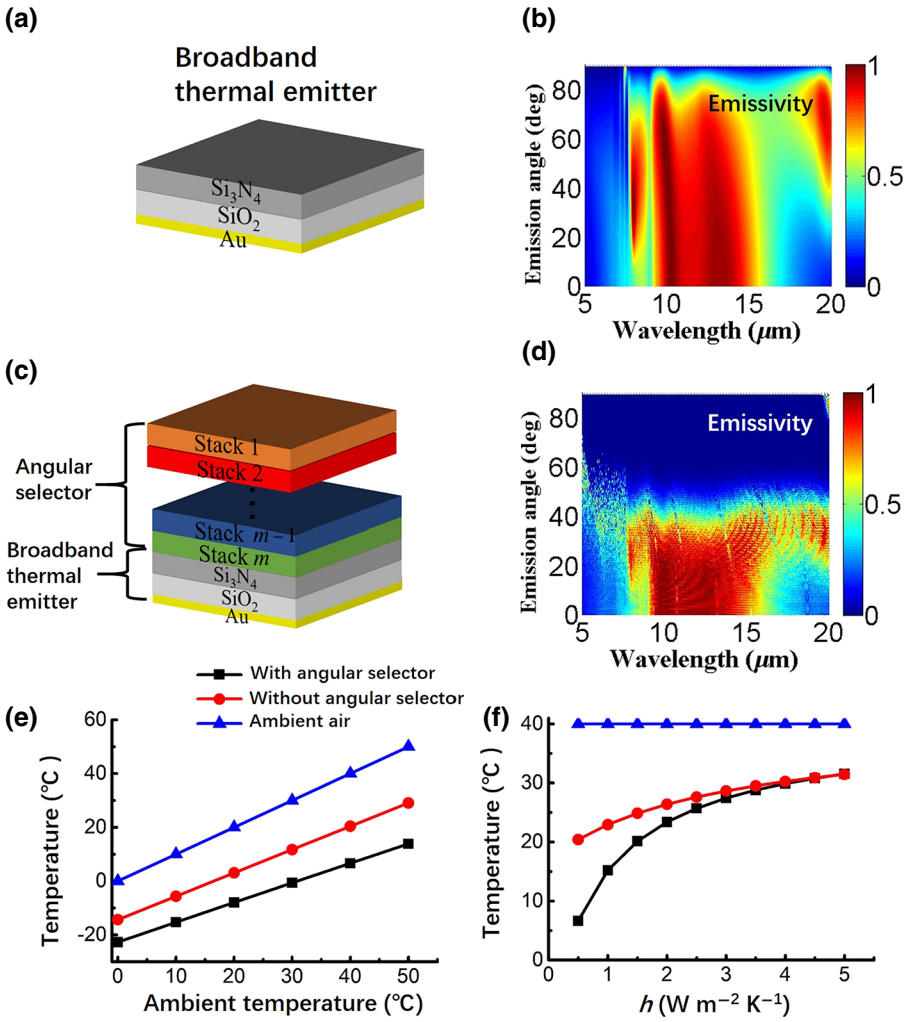

FIG. 4. (a) A three-layer broadband thermal emitter consisting of Au, SiO_2, and Si_3N_4 films. (b) The emissivities of the three-layer broadband thermal emitter. (c) A DBTE consisting of a broadband thermal emitter at the bottom and a multilayer angular selector on the top. The angular selector consists of 160 stacks, each stack consisting of 60 isotropic-anisotropic bilayers. (d) The emissivities of the DBTE. (e) The equilibrium temperatures of ambient air (blue line), the broadband thermal emitter (red line), and the DBTE (black line) for different ambient temperatures. The effective heat-transfer coefficient $h = 0.5\ \mathrm{W\,m^{-2}\,K^{-1}}$. (f) The equilibrium temperatures of ambient air, the broadband thermal emitter, and the DBTE for different effective heat-transfer coefficients h.

reflection from 40° to 90° [Fig. 4(d)]. The "emission-window" size of the DBTE can be tuned by changing the number of bilayers.

The equilibrium temperatures of ambient air, the broadband thermal emitter, and the DBTE are calculated on the basis of the method described in Appendix B. Both the broadband thermal emitter (without an angular selector) and the DBTE (with an angular selector) can decrease the temperatures of the samples through radiative cooling, as shown in Fig. 4(e). The DBTE with an angular selector shows better radiative-cooling performance than the broadband thermal emitter without an angular selector. For example, the temperature of the DBTE is around 12 °C lower than that of the broadband thermal emitter when the ambient temperature is 30 °C. Here we choose the effective heat-transfer coefficient h as $0.5\ \mathrm{W\,m^{-2}\,K^{-1}}$. With the help of low-conductivity materials and a high vacuum (10^{-6} Torr), the effective heat-transfer coefficient h can be further reduced to the range 0.2–0.3 $\mathrm{W\,m^{-2}\,K^{-1}}$ [50].

The effective heat-transfer coefficient has an obvious effect on the radiative-cooling performance of the sample. As shown in Fig. 4(f), the cooling temperatures increase for both the broadband thermal emitter and the DBTE when the heat-transfer coefficient is increased. At the same time, the difference in the cooling temperatures between the broadband thermal emitter and the DBTE decreases. The temperatures of the broadband thermal emitter and the DBTE are almost the same when the heat-transfer coefficient h is increased to $5\ \mathrm{W\,m^{-2}\,K^{-1}}$. The reason is that the temperature of the sample increases and becomes close to the ambient temperature when h is increased. The difference between the thermal emission from the buildings and that from the sample is small, and therefore the advantage of the angular selector is not so obvious. On the other hand, covering the broadband thermal emitter with an angular selector decreases the whole emissivities of the DBTE to some extent. As a result, the temperatures of the broadband thermal emitter and the DBTE are almost the same when the heat-transfer coefficient h is large. The equilibrium temperatures of ambient air, the broadband thermal emitter, and the DBTE are calculated for different values of θ_b (see Fig. S5 in Supplemental Material [49]).

III. DIRECTIONAL AND NARROWBAND THERMAL EMITTER

A. Structure and emissivities of the DNTE

We now discuss how to achieve a DNTE. We design a material system that contains an angular selector on top of a vertical-cavity enhanced resonant thermal emitter [22]. The vertical-cavity enhanced resonant thermal emitter consists of seven bilayers of ZnS films (low refractive index) and Si films (high refractive index) on top of a 100-nm-thick gold film [Fig. 5(a)]. The thicknesses of the ZnS and Si films are 500 and 300 nm, respectively. The vertical-cavity enhanced resonant thermal emitter is a typical spatially and temporally coherent thermal emitter, which has narrowband thermal emission at a specific emission angle, as shown in Figs. 5(c) and 5(f). To achieve

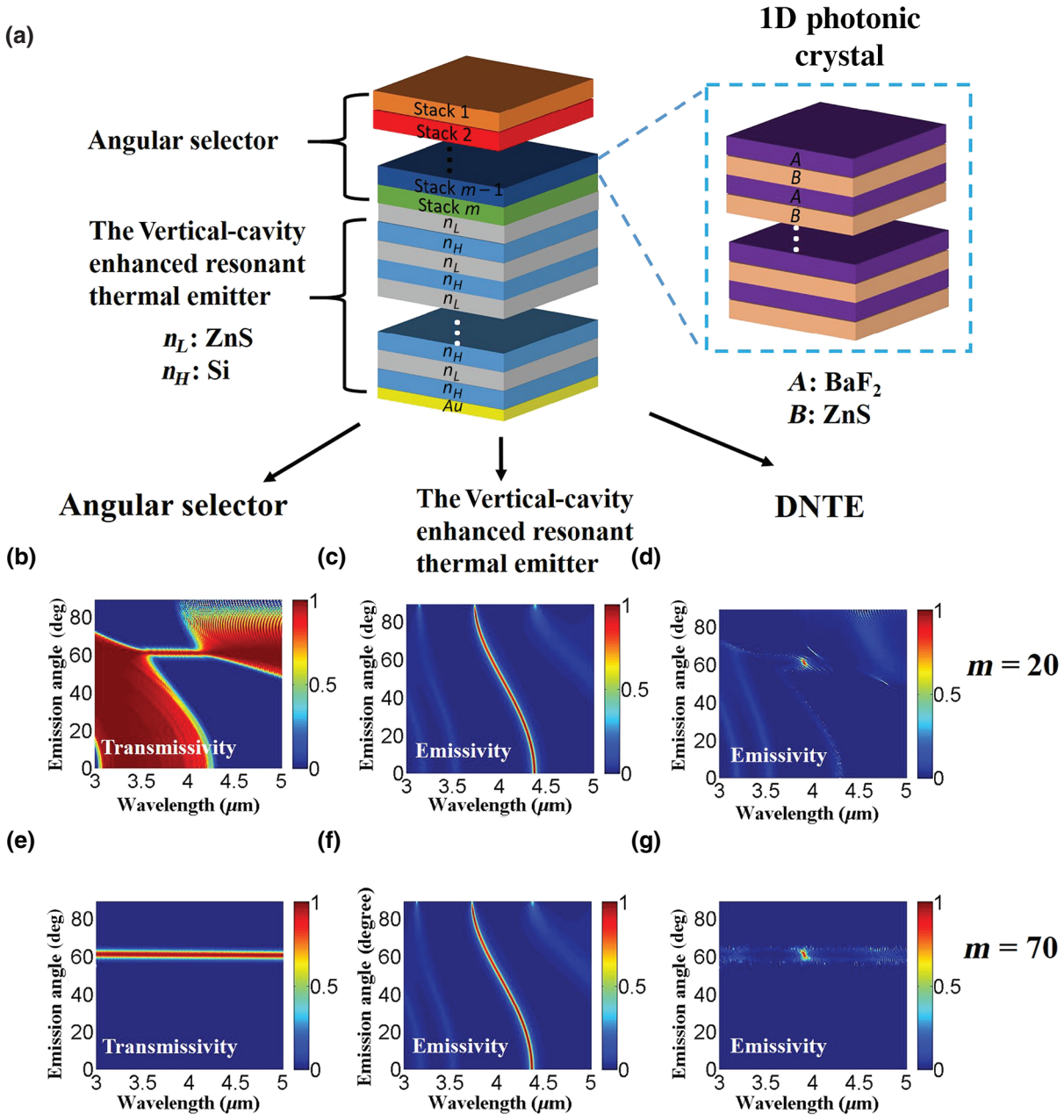

FIG. 5. (a) The DNTE contains an angular selector on top of a vertical-cavity enhanced resonant thermal emitter. (b)–(d) p-polarized transmissivity of the angular selector and emissivities of the vertical-cavity enhanced resonant thermal emitter and the DNTE. The angular selector consists of 20 stacks ($m = 20$), each stack consisting of ten bilayers. (e)–(g) p-polarized transmissivity of the angular selector and emissivities of the vertical-cavity enhanced resonant thermal emitter and the DNTE. The angular selector consists of 70 stacks ($m = 70$), each stack consisting of ten bilayers. All the materials in our simulation are widely used: Au, ZnS, BaF_2, and Si.

spatial and temporal confinement of thermal emission, we add an angular selector on top of the vertical-cavity enhanced resonant thermal emitter [Fig. 5(a)]. Only the thermal emission within the transparent window of the angular selector can escape and the thermal emission from other angles will be reflected back and suppressed.

We design two angular selectors with different transparent-window sizes that can be controlled by the number of stacks m. One angular selector contains 20 stacks, each stack consisting of ten bilayers, as shown in Fig. 5(b). The periods of these stacks form a geometric series $a_i = a_0 r^{i-1}$ with $a_0 = 650$ nm and $r = 1.01$. The other angular selector contains 70 stacks, each stack consisting of ten bilayers, as shown in Fig. 5(e). The periods of these stacks form a geometric series $a_i = a_0 r^{i-1}$ with $a_0 = 530$ nm and $r = 1.01$. We demonstrate that a DNTE can be achieved as long as the emission peak of the vertical-cavity enhanced resonant thermal emitter falls in the transparent window of the angular selector, as shown in Figs. 5(d) and 5(g). However, the angular selectors with different numbers of stacks m have different performances, which is discussed in detail later. The temperature-dependent emissivity of the DNTE is also studied considering the refractive index of Si is temperature dependent (see Appendix A). When the temperature increases to 1000 K, several modes can be excited simultaneously, and thus the thermal emission from other wavelengths increases, as shown in Fig. S7 in Supplemental Material [49].

B. Application of the DNTE in high-efficiency infrared light sources

High energy-conversion efficiency is of vital importance to achieve high-efficiency infrared light sources. We demonstrate that the energy-conversion efficiency can be increased if an angular selector is applied to the vertical-cavity enhanced resonant thermal emitter. We use two different models to calculate equilibrium temperatures and the spectral radiance of a black body, the vertical-cavity enhanced resonant thermal emitter, and the DNTE when the input power is fixed, as shown in Figs. 6(a) and S8(a). In Fig. 6(a), we assume that the device is in a vacuum. Conduction and convection are negligible. The input power can be totally converted to heat and this increases the temperatures of the three kinds of devices. The equilibrium temperatures of the three kinds of devices can be calculated on the basis of conservation of energy (see Appendix C). The vertical-cavity enhanced resonant thermal emitter is the same as that shown in Fig. 5(a). The narrowband-thermal-emitter part of the DNTE is the same as that shown in Fig. 5(a), while the angular-selector part is different, with 70 stacks ($a_0 = 650$ nm and $r = 1.03$), each stack consisting of ten bilayers.

We compare the equilibrium temperatures of a black body, the vertical-cavity enhanced resonant thermal emitter, and the DNTE in Fig. 6(b). With the same input power (50 mW), the DNTE reaches the highest equilibrium temperature and the temperature of the black body is the lowest. The spectral radiance is calculated at an emission angle

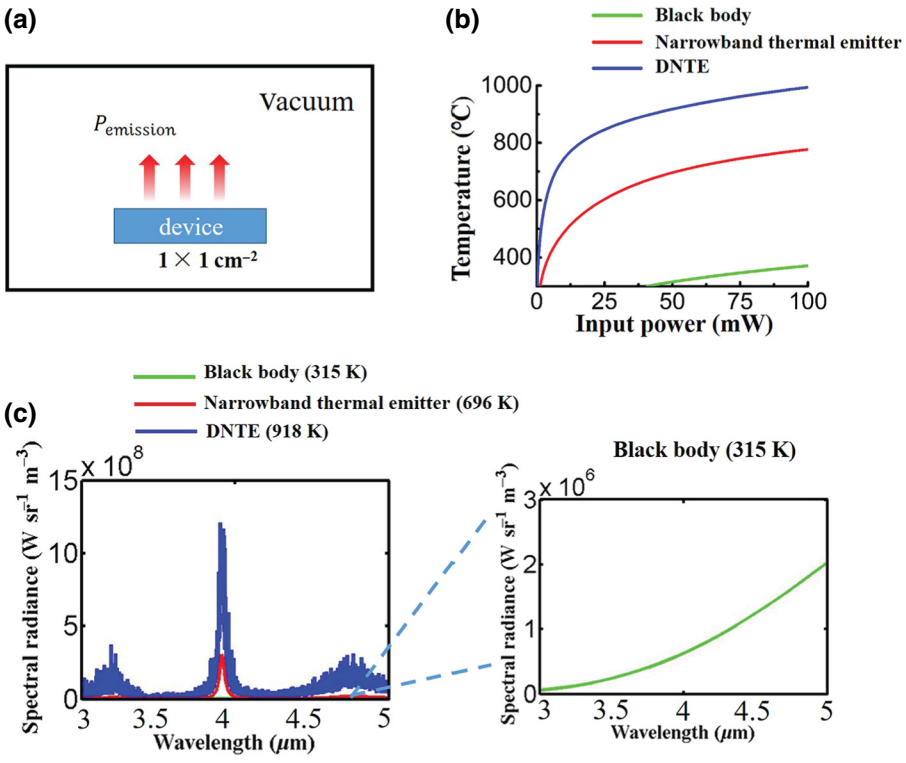

FIG. 6. (a) Model of the device in a vacuum. We assume conduction and convection are negligible. (b) The equilibrium temperatures for a black body (green line), a narrowband thermal emitter (red line), and the DNTE (blue line) for different input powers. Here the narrowband thermal emitter is a vertical-cavity enhanced resonant thermal emitter. (c) The spectral radiance for a black body, a narrowband thermal emitter, and the DNTE at an emission angle of 60° when the input power is the same (50 mW). We zoom in the radiance of black body because it is much smaller compared to that of narrowband thermal emitter and DNTE.

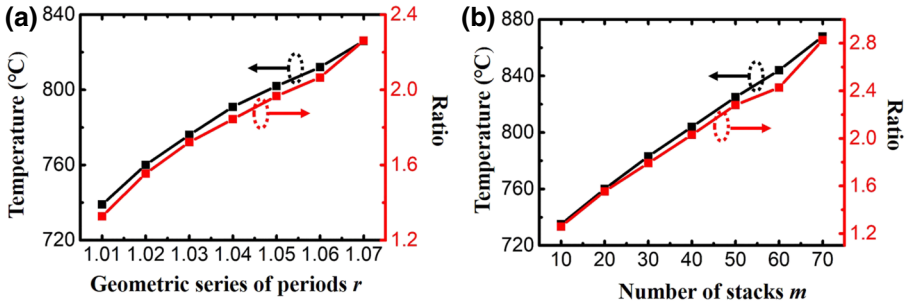

FIG. 7. Equilibrium temperatures and the ratio of the spectral radiance of the DNTE to that of the vertical-cavity enhanced resonant thermal emitter for (a) different geometric series of periods r when the number of stacks m is 20 and for (b) different numbers of stacks m when the geometric series of periods r is 1.02. The input power is 50 mW.

of 60° for the three kinds of thermal emitters, as shown in Fig. 6(c). The black body exhibits the lowest radiance in 3–5 μm, around 2–3 orders of magnitudes lower than that of the other kinds of thermal emitters. The peak radiance of the DNTE is around 12×10^8 W sr^{-1} m^{-3}, 4 times higher than that of vertical-cavity enhanced resonant thermal emitter (3×10^8 W sr^{-1} m^{-3}). These results demonstrate that the DNTE with both spatial and temporal confinement can reach a higher equilibrium temperature and peak radiance at the objective wavelength of 3.9 μm and emission angle of 60° with the same input power. The emissivities of the DNTE at different emission angles are investigated at a fixed emission wavelength of 3.9 μm (see Fig. S9 in Supplemental Material [49]). The thermal emission of the DNTE is highly directional, with an emission-angle width of around 2°.

C. Effect of geometric parameters on the final energy-conversion performance

Both the geometric series of periods r and the number of stacks m have an effect on the equilibrium temperatures and the spectral radiance of the devices. Here we use the radiance of the vertical-cavity enhanced resonant thermal emitter (R_{base}) as the baseline and calculate the ratio of the radiance of the DNTE structure (R_{DNTE}) to R_{base}. A large geometric series of periods r leads to high equilibrium temperatures and high spectral radiance of the DNTE [Fig. 7(a)]. The case for the number of stacks m is almost the same [Fig. 7(b)]. The reason is that the location of the band gap scales proportionally to the period of the quarter-wave stack. The large geometric series of periods r and number of stacks m result in a large transparent-window size, which can suppress the wasted thermal emission in a broadband wavelength range. Therefore, high energy-conversion efficiency can be realized. These results can guide us to design a proper thermal emitter considering the trade-off between the energy-conversion efficiency and the fabrication complexity.

IV. CONCLUSION

In conclusion, we propose two kinds of thermal emitters, a DBTE and a DNTE, based on a classic thermal emitter combined with an angular selector. We study not only fundamental problems such as how to control the spatial and spectral properties of thermal emission, but also a number of practical applications. The DBTE can control the direction of thermal emission in a broadband range, while the DNTE can control the direction of thermal emission in a narrowband range. From the view of band diagrams, the angular selectivity can be achieved because the extended modes can exist within the band gaps at the Brewster angle. For a photonic crystal without the Brewster angle, no modes are allowed to propagate within the band gaps (see Fig. S10 in Supplemental Material [49]). The DBTE can achieve lower radiative-cooling temperatures than classic thermal emitters without angular control when there are surrounding buildings. The DNTE exhibits higher energy-conversion efficiency than the conventional narrowband thermal emitter. We systematically study the effect of a geometric series of periods r and the number of stacks m on the equilibrium temperature and the spectral radiance, which is useful guidance to design a proper DNTE. The proposed DBTE and DNTE can directionally and spectrally control thermal emission and significantly benefit a number of applications such as thermophotovoltaic devices, radiative cooling, and high-efficiency infrared light sources. One natural next step is to study the dynamic control of the direction and wavelength of thermal emission, which can be realized by use of liquid-crystal or phase-changing materials.

ACKNOWLEDGMENTS

We are grateful to Professor Marin Soljačić and Dr. Ivan Celanovic at MIT for helpful discussions. This project was supported by the National Key Research and Development Program of China (Grant No. 2017YFA0205700) and the National Natural Science Foundation of China (Grant No. 61927820).

APPENDIX A: MATERIALS

In our simulations, the permittivity of ZnS $\varepsilon_{\text{ZnS}} = 8.393 + 0.14383/(\lambda^2 - 0.2421^2) + 4430.99/(\lambda^2 - 36.71^2)$ [51] and the permittivity of BaF2 $\varepsilon_{\text{BaF2}} = 1.33973 + 0.8107\lambda^2/(\lambda^2 - 0.10065^2) + 0.19652\lambda^2/(\lambda^2 - 29.87^2) + 4.52469\lambda^2/(\lambda^2 - 53.82^2)$ [52]. The temperature-dependent

absorption of Si can be modeled by means of the absorption coefficient [53]: $\alpha_{\rm si} = 4.15 \times 10^{-5}\lambda^{1.51}T^{2.95}\exp(-7000/T)$, where λ is in micrometers, T is in kelvins, and α is in reciprocal centimeters. The real part of the refractive index of Si is assumed to be temperature independent, $n_{\rm Si} = 3.34$. The permittivity of Au is modeled by the Drude model [54] as $\varepsilon_{\rm Au}(\omega) = \varepsilon_1(\omega) + i\varepsilon_2(\omega) = 1 - \omega_p^2/(\omega^2 + i\Gamma\omega)$, where $\hbar\omega_p = 8.5$ and $\tau_D = 1/\Gamma = 14$ fs.

APPENDIX B: METHOD FOR THE CALCULATION OF THE EQUILIBRIUM TEMPERATURE OF RADIATIVE COOLING

The energy flux of the device contains three parts: thermal emission P_r, absorption from the atmosphere and buildings P_a, and conductive and convective loss P_c. The thermal-emission part P_r of the device is described as follows:

$$\begin{aligned} P_r &= \iiint \varepsilon_s(\theta,\omega) \times I_{\rm BB}(\omega, T_s)\cos\theta\sin\theta d\theta d\varphi d\omega \\ &= \iiint \varepsilon_s(\theta,\omega) \times \frac{2hc^2}{\lambda^5}\frac{1}{\exp(hc/\lambda k_B T_s) - 1} \\ &\quad \times \cos\theta\sin\theta d\theta d\varphi d\omega, \end{aligned} \tag{B1}$$

where ε_s is the emissivity of the device, $I_{\rm BB}$ is the theoretical black-body radiance, and T_s is the temperature of the device. The absorption of the device contains two parts: thermal emission from the ambient atmosphere $P_{\rm atm}$ and from the surrounding buildings P_b:

$$\begin{aligned} P_a &= P_{\rm atm} + P_b \\ &= \iiint \varepsilon_s(\theta,\omega) \times I_{\rm BB}(\omega, T_a) \\ &\quad \times \varepsilon_{\rm atm}(\theta,\omega)\cos\theta\sin\theta d\theta d\varphi d\omega \\ &\quad + \iiint \varepsilon_s(\theta,\omega) \\ &\quad \times I_{\rm BB}(\omega, T_a) \times \varepsilon_b(\theta,\omega)\cos\theta\sin\theta d\theta d\varphi d\omega, \end{aligned}$$

where $\varepsilon_{\rm atm}$ is the emissivity of the ambient atmosphere, ε_b is the emissivity of the buildings, and T_a is the ambient temperature. The last part is the heat-transfer part P_c including conduction and convection:

$$P_c = h \times (T_S - T_a), \tag{B2}$$

where h is effective heat-transfer coefficient. The equilibrium temperature can be calculated when the net energy flux $P_{\rm net}$ is zero:

$$P_{\rm net} = P_a + P_c - P_r = 0. \tag{B3}$$

APPENDIX C: METHODS FOR THE CALCULATION OF THE EQUILIBRIUM TEMPERATURE OF THE INFRARED LIGHT SOURCE

In the first model, a constant input power $P_{\rm in}$ is applied to the device. The initial temperature of the device is low, and then the temperature starts to increase until the steady state, namely, $P_{\rm in} = P_{\rm out}$, is reached. $P_{\rm out}$ is the power that emits from the device to the environment through thermal emission, where conduction and convection are ignored. The temperature-dependent and angular-resolved emissivities $\varepsilon(\theta,\omega,T)$ of the vertical-cavity enhanced resonant thermal emitter and the DNTE are shown in Fig. S7. $I_{\rm BB}(\theta,\omega,T)$ is the theoretical black-body radiance (Lambert radiator). By temporally and spatially integrating the thermal emission of the device, we can obtain the input power $P_{\rm in}$ as follows:

$$\begin{aligned} P_{\rm in} &= \iiint \varepsilon(\theta,\omega,T) \times I_{\rm BB}(\theta,\omega,T)\cos\theta\sin\theta d\theta d\varphi d\omega \\ &= \iiint \varepsilon(\theta,\omega,T) \times \frac{2hc^2}{\lambda^5}\frac{1}{\exp(hc/\lambda k_B T) - 1} \\ &\quad \times \cos\theta\sin\theta d\theta d\varphi d\omega. \end{aligned} \tag{C1}$$

For a fixed input power $P_{\rm in}$, the equilibrium temperature of the device can be calculated with the above formula.

In the second model, we consider the thermal-conduction loss due to the metal wires. We choose Manganin wires, which have a relatively low thermal conductivity ($k = 7.81\ {\rm W}^{-1}\,{\rm K}^{-1}$), to minimize the conduction loss. The diameter and length of the manganin wires are 400 μm and 10 mm, respectively. At steady state, the equilibrium temperature of the device can be calculated with the following the formula:

$$P_{\rm in} = P_{\rm emission} + P_{\rm cond} = P_{\rm emission} + kA_{\rm wire}\frac{T - T_0}{L_{\rm wire}}, \tag{C2}$$

where k is the thermal conductivity of the wire, $A_{\rm wire}$ and $L_{\rm wire}$ are the cross-section area and length of the wire, respectively, T is the equilibrium temperature of the device, and T_0 is the environmental temperature.

[1] Rémi Carminati and Jean-Jacques Greffet, Near-Field Effects in Spatial Coherence of Thermal Sources, Phys. Rev. Lett. **82**, 1660 (1999).

[2] Jean-Jacques Greffet, Rémi Carminati, Karl Joulain, Jean-Philippe Mulet, Stéphane Mainguy, and Yong Chen, Coherent emission of light by thermal sources, Nature **416**, 61 (2002).

[3] Aaswath P. Raman, Marc Abou Anoma, Linxiao Zhu, Eden Rephaeli, and Shanhui Fan, Passive radiative cooling below

ambient air temperature under direct sunlight, Nature **515**, 540 (2014).

[4] Yao Zhai, Yaoguang Ma, Sabrina N. David, Dongliang Zhao, Runnan Lou, Gang Tan, Ronggui Yang, and Xiaobo Yin, Scalable-manufactured randomized glass-polymer hybrid metamaterial for daytime radiative cooling, Science **355**, 1062 (2017).

[5] Bikram Bhatia, Arny Leroy, Yichen Shen, Lin Zhao, Melissa Gianello, Duanhui Li, Tian Gu, Juejun Hu, Marin Soljačić, and Evelyn N. Wang, Passive directional sub-ambient daytime radiative cooling, Nat. Commun. **9**, 5001 (2018).

[6] Po-Chun Hsu, Alex Y. Song, Peter B. Catrysse, Chong Liu, Yucan Peng, Jin Xie, Shanhui Fan, and Yi Cui, Radiative human body cooling by nanoporous polyethylene textile, Science **353**, 1019 (2016).

[7] Lyu Zhou, Haomin Song, Jianwei Liang, Matthew Singer, Ming Zhou, Edgars Stegenburgs, Nan Zhang, Chen Xu, Tien Ng, and Zongfu Yu, *et al.*, A polydimethylsiloxane-coated metal structure for all-day radiative cooling, Nat. Sustainability **2**, 718 (2019).

[8] Andrej Lenert, David M. Bierman, Youngsuk Nam, Walker R. Chan, Ivan Celanović, Marin Soljačić, and Evelyn N. Wang, A nanophotonic solar thermophotovoltaic device, Nat. Nanotechnol. **9**, 126 (2014).

[9] Takashi Asano, Masahiro Suemitsu, Kohei Hashimoto, Menaka De Zoysa, Tatsuya Shibahara, Tatsunori Tsutsumi, and Susumu Noda, Near-infrared–to–visible highly selective thermal emitters based on an intrinsic semiconductor, Sci. Adv. **2**, e1600499 (2016).

[10] Pavel N. Dyachenko, Sean Molesky, A. Yu Petrov, Michael Störmer, Tobias Krekeler, Slawa Lang, Martin Ritter, Zubin Jacob, and Manfred Eich, Controlling thermal emission with refractory epsilon-near-zero metamaterials via topological transitions, Nat. Commun. **7**, 11809 (2016).

[11] Yurui Qu, Qiang Li, Lu Cai, Meiyan Pan, Pintu Ghosh, Kaikai Du, and Min Qiu, Thermal camouflage based on the phase-changing material gst, Light: Sci. Appl. **7**, 26 (2018).

[12] Ying Li, Xue Bai, Tianzhi Yang, Hailu Luo, and Cheng-Wei Qiu, Structured thermal surface for radiative camouflage, Nat. Commun. **9**, 273 (2018).

[13] Mikhail A. Kats, Romain Blanchard, Shuyan Zhang, Patrice Genevet, Changhyun Ko, and Shriram Ramanathan, and Federico Capasso, Vanadium Dioxide as a Natural Disordered Metamaterial: Perfect Thermal Emission and Large Broadband Negative Differential Thermal Emittance, Phys. Rev. X **3**, 041004 (2013).

[14] Lin Xiao, He Ma, Junku Liu, Wei Zhao, Yi Jia, Qiang Zhao, Kai Liu, Yang Wu, Yang Wei, Shoushan Fan, *et al.*, Fast adaptive thermal camouflage based on flexible vo2/graphene/cnt thin films, Nano Lett. **15**, 8365 (2015).

[15] Menaka De Zoysa, Takashi Asano, Keita Mochizuki, Ardavan Oskooi, Takuya Inoue, and Susumu Noda, Conversion of broadband to narrowband thermal emission through energy recycling, Nat. Photonics **6**, 535 (2012).

[16] D. Costantini, Antoine Lefebvre, A.-L. Coutrot, I. Moldovan-Doyen, J.-P. Hugonin, S. Boutami, F. Marquier, H. Benisty, and J.-J. Greffet, Plasmonic Metasurface for Directional and Frequency-Selective Thermal Emission, Phys. Rev. Appl. **4**, 014023 (2015).

[17] Wei Wang, Yurui Qu, Kaikai Du, Songang Bai, Jingyi Tian, Meiyan Pan, Hui Ye, Min Qiu, and Qiang Li, Broadband optical absorption based on single-sized metal-dielectric-metal plasmonic nanostructures with high-ε'' metals, Appl. Phys. Lett. **110**, 101101 (2017).

[18] Xianliang Liu, Talmage Tyler, Tatiana Starr, Anthony F. Starr, Nan Marie Jokerst, and Willie J. Padilla, Taming the Blackbody with Infrared Metamaterials as Selective Thermal Emitters, Phys. Rev. Lett. **107**, 045901 (2011).

[19] Yurui Qu, Qiang Li, Kaikai Du, Lu Cai, Jun Lu, and Min Qiu, Dynamic thermal emission control based on ultrathin plasmonic metamaterials including phase-changing material gst, Laser Photon. Rev. **11**, 1700091 (2017).

[20] Alexander Lochbaum, Yuriy Fedoryshyn, Alexander Dorodnyy, Ueli Koch, Christian Hafner, and Juerg Leuthold, On-chip narrowband thermal emitter for mid-ir optical gas sensing, ACS Photonics **4**, 1371 (2017).

[21] Yurui Qu, Qiang Li, Hanmo Gong, Kaikai Du, Songang Bai, Ding Zhao, Hui Ye, and Min Qiu, Spatially and spectrally resolved narrowband optical absorber based on 2d grating nanostructures on metallic films, Adv. Opt. Mater. **4**, 480 (2016).

[22] Ivan Celanovic, David Perreault, and John Kassakian, Resonant-cavity enhanced thermal emission, Phys. Rev. B **72**, 075127 (2005).

[23] B. J. Lee, C. J. Fu, and Z. M. Zhang, Coherent thermal emission from one-dimensional photonic crystals, Appl. Phys. Lett. **87**, 071904 (2005).

[24] Grégory Barbillon, Emilie Sakat, Jean-Paul Hugonin, Svend-Age Biehs, and Philippe Ben-Abdallah, True thermal antenna with hyperbolic metamaterials, Opt. Express **25**, 23356 (2017).

[25] O. G. Kollyukh, A. I. Liptuga, V. Morozhenko, and V. I. Pipa, Thermal radiation of plane-parallel semitransparent layers, Opt. Commun. **225**, 349 (2003).

[26] Christos Argyropoulos, Khai Q. Le, Nadia Mattiucci, Giuseppe D'Aguanno, and Andrea Alu, Broadband absorbers and selective emitters based on plasmonic brewster metasurfaces, Phys. Rev. B **87**, 205112 (2013).

[27] S. E. Han and David J. Norris, Beaming thermal emission from hot metallic bull's eyes, Opt. Express **18**, 4829 (2010).

[28] Salvatore Campione, Francois Marquier, Jean-Paul Hugonin, A. Robert Ellis, John F. Klem, Michael B. Sinclair, and Ting S. Luk, Directional and monochromatic thermal emitter from epsilon-near-zero conditions in semiconductor hyperbolic metamaterials, Sci. Rep. **6**, 34746 (2016).

[29] Linxiao Zhu, Fengyuan Liu, Hongtao Lin, Juejun Hu, Zongfu Yu, Xinran Wang, and Shanhui Fan, Angle-selective perfect absorption with two-dimensional materials, Light: Sci. Appl. **5**, e16052 (2016).

[30] Yichen Shen, Dexin Ye, Ivan Celanovic, Steven G. Johnson, John D. Joannopoulos, and Marin Soljačić, Optical broadband angular selectivity, Science **343**, 1499 (2014).

[31] Yurui Qu, Yichen Shen, Kezhen Yin, Yuanqing Yang, Qiang Li, Min Qiu, and Marin Soljačić, Polarization-independent optical broadband angular selectivity, ACS Photonics **5**, 4125 (2018).

[32] O. Höhn, M. Peters, C. Ulbrich, A. Hoffmann, U. T. Schwarz, and B. Bläsi, in *Photonics for Solar Energy*

Systems IV (International Society for Optics and Photonics, Brussels, Belgium, 2012), Vol. 8438, p. 84380A.

[33] Emily D. Kosten, Jackson H. Atwater, James Parsons, Albert Polman, and Harry A. Atwater, Highly efficient gaas solar cells by limiting light emission angle, Light: Sci. Appl. **2**, e45 (2013).

[34] Steven William Macmaster, Privacy screen for a display, US Patent 7, 052, 746 (2006).

[35] Graham M. Clarke, Paul D. Graham, Brent R. Hansen, Travis B. Hoium, and David F. Slama, Privacy film, US Patent 7, 467, 873 (2008).

[36] Yichen Shen, Chia Wei Hsu, Yi Xiang Yeng, John D. Joannopoulos, and Marin Soljačić, Broadband angular selectivity of light at the nanoscale: Progress, applications, and outlook, Appl. Phys. Rev. **3**, 011103 (2016).

[37] Fumio Nagatoshi and Tamio Arakawa, Structure of doubly oriented nylon 6, Polym. J. **1**, 685 (1970).

[38] Mukerrem Cakmak, James L. White, and Joseph E. Spruiell, Optical properties of simultaneous biaxially stretched poly (ethylene terephthalate) films, Polym. Eng. Sci. **29**, 1534 (1989).

[39] J. A. Van Aken and H. Janeschitz-Kriegl, Simultaneous measurement of transient stress and flow birefringence in one-sided compression (biaxial extension) of a polymer melt, Rheol. Acta **20**, 419 (1981).

[40] Gudrun Schmidt, Alan I. Nakatani, Paul D. Butler, Alamgir Karim, and Charles C. Han, Shear orientation of viscoelastic polymer- clay solutions probed by flow birefringence and sans, Macromolecules **33**, 7219 (2000).

[41] Kezhen Yin, Zheng Zhou, Donald E. Schuele, Mason Wolak, Lei Zhu, and Eric Baer, Effects of interphase modification and biaxial orientation on dielectric properties of poly (ethylene terephthalate)/poly (vinylidene fluoride-co-hexafluoropropylene) multilayer films, ACS Appl. Mater. Interfaces **8**, 13555 (2016).

[42] Hongwen Ren and Shin-Tson Wu, Tunable electronic lens using a gradient polymer network liquid crystal, Appl. Phys. Lett. **82**, 22 (2003).

[43] Walter J. Schrenk, Douglas S. Chisholm, Kenneth J. Cleereman, and Turner Alfrey, Jr., Method of preparing multilayer plastic articles, US Patent 3, 565, 985 (1971).

[44] Turner Alfrey, Jr. and Walter J. Schrenk, Multilayer coextrusion process for producing selective reflectivity, US Patent 4, 094, 947 (1978).

[45] Richard A. Kollaja, Axel Eckstein, and Robert M. Floyd, Polymeric coextruded multilayer articles US Patent 6, 949, 283 (2005).

[46] Craig F. Culver, Interface control, US Patent 5, 666, 138 (1997).

[47] Richard Y. F. Liu, Yi Jin, Anne Hiltner, and Eric Baer, Probing nanoscale polymer interactions by forced-assembly, Macromol. Rapid. Commun. **24**, 943 (2003).

[48] You Wang, Yukio Abe, Yuji Matsuura, Mitsunobu Miyagi, and Hiroshi Uyama, Refractive indices and extinction coefficients of polymers for the mid-infrared region, Appl. Opt. **37**, 7091 (1998).

[49] See Supplemental Material at http://link.aps.org/supplemental/10.1103/PhysRevApplied.13.064052 for the figures.

[50] Zhen Chen, Linxiao Zhu, Aaswath Raman, and Shanhui Fan, Radiative cooling to deep sub-freezing temperatures through a 24-h day–night cycle, Nat. Commun. **7**, 13729 (2016).

[51] Claude A. Klein, Room-temperature dispersion equations for cubic zinc sulfide, Appl. Opt. **25**, 1873 (1986).

[52] H. H. Li, Refractive index of alkaline earth halides and its wavelength and temperature derivatives, J. Phys. Chem. Ref. Data **9**, 161 (1980).

[53] Peter Vandenabeele and Karen Maex, Influence of temperature and backside roughness on the emissivity of si wafers during rapid thermal processing, J. Appl. Phys. **72**, 5867 (1992).

[54] Robert L. Olmon, Brian Slovick, Timothy W. Johnson, David Shelton, Sang-Hyun Oh, Glenn D. Boreman, and Markus B. Raschke, Optical dielectric function of gold, Phys. Rev. B **86**, 235147 (2012).